

The broad-band SEDs of four ‘hypervariable’ AGN

James S. Collinson,^{1★} Martin J. Ward,^{1★} Andy Lawrence,^{2★} Alastair Bruce,²
Chelsea L. MacLeod,³ Martin Elvis,³ Suvi Gezari,⁴ Philip J. Marshall⁵
and Chris Done¹

¹Centre for Extragalactic Astronomy, Department of Physics, Durham University, South Road, Durham DH1 3LE, UK

²Institute for Astronomy, SUPA (Scottish Universities Physics Alliance), University of Edinburgh, Royal Observatory, Blackford Hill, Edinburgh EH9 3HJ, UK

³Harvard–Smithsonian Center for Astrophysics, 60 Garden St., Cambridge, MA 02138, USA

⁴Department of Astronomy, University of Maryland, Stadium Drive, College Park, MD 20742-2421, USA

⁵Kavli Institute for Particle Astrophysics and Cosmology, PO Box 20450, MS 29, Stanford, CA 94309, USA

Accepted 2017 November 17. Received 2017 November 17; in original form 2015 December 2

ABSTRACT

We present an optical-to-X-ray spectral analysis of four ‘hypervariable’ AGN (HVAs) discovered by comparing Pan-STARRS data to that from the Sloan Digital Sky Survey over a 10 yr baseline (Lawrence et al.). There is some evidence that these objects are X-ray loud for their corresponding UV luminosities, but given that we measured them in a historic high state, it is not clear whether to take the high state or low state as typical of the properties of these HVAs. We estimate black hole masses based on Mg II and H α emission line profiles, and either the high- or low-state luminosities, finding mass ranges $\log(M_{\text{BH}}/M_{\odot}) = 8.2\text{--}8.8$ and $\log(M_{\text{BH}}/M_{\odot}) = 7.9\text{--}8.3$, respectively. We then fit energy-conserving models to the spectral energy distributions (SEDs), obtaining strong constraints on the bolometric luminosity and α_{OX} . We compare the SED properties with a larger, X-ray selected AGN sample for both of these scenarios, and observe distinct groupings in spectral shape versus luminosity parameter space. In general, the SED properties are closer to normal if we assume that the low state is representative. This supports the idea that the large slow outbursts may be due to extrinsic effects (for example microlensing) as opposed to accretion rate changes, but a larger sample of HVAs is needed to be confident of this conclusion.

Key words: accretion, accretion discs – black hole physics – gravitational lensing: micro – galaxies: active.

1 INTRODUCTION

1.1 Background

Based on variability, luminosity, and multi-frequency spectral energy distributions (SEDs), it is now accepted that gas accretion on to central galactic supermassive black holes (BHs) is the mechanism by which large amounts of energy are radiated from active galactic nuclei (AGN). We can probe these objects spectroscopically and temporally, as they emit across a great range of energies and exhibit variability at many frequencies (e.g. Salpeter 1964; Ward et al. 1987; Cristiani, Vio & Andreani 1990; Alexander & Hickox 2012; Collinson 2016).

In an earlier paper (Lawrence et al. 2016, hereafter L16), we described the discovery of a large sample of ‘hypervariable AGN (HVAs)’. A search was made, originally for variable tidal disruption

event (TDE; e.g. Rees 1988) candidates, in the Panoramic Survey Telescope And Rapid Response System (Pan-STARRS) data base, which repeatedly surveys large regions of the sky with high cadence, and is therefore well suited to searches for variable objects (e.g. Gezari et al. 2012; Morganson et al. 2015). Pan-STARRS detections were compared to the ~ 10 yr earlier Sloan Digital Sky Survey (SDSS) measurements, and objects that had undergone a large increase in brightness ($|\Delta m| > 1.5$ mag in at least one optical filter) were selected as candidates. In addition to TDE and central region supernova (SN) candidates, this search yielded a significant number of very blue objects that follow-up photometry showed to be evolving on time-scales of several years, whereas SNe and TDEs typically fade over time periods of weeks to months (L16). Moreover, many of these slow, blue, variable objects were still increasing in brightness. Spectroscopy revealed them to be AGN at moderate redshifts ($z \sim 1$). Such extreme variability is rare for AGN, leading us to explore the possible explanations for these HVAs. Our definition of ‘hypervariable’ here differs from that in Morganson et al. (2015); that study defines all objects with $|\Delta m| > 2$ mag as ‘hypervariable’, and as such includes a large number of highly variable stars and other phenomena, in addition to some AGN.

* E-mail: j.s.collinson@durham.ac.uk (JSC); martin.ward@durham.ac.uk (MJW); al@roe.ac.uk (AL)

1.2 Possible mechanisms for HVAs

L16 examined the properties of this growing sample of HVAs (currently 76 objects) and considered several interpretations of the data. These included highly luminous, slowly evolving TDEs, line-of-sight extinction changes, extreme accretion rate changes, and foreground microlensing.

L16 noted that the TDE explanation requires unusually massive stars ($\sim 10 M_{\odot}$) to be torn apart by the BH tidal forces to satisfactorily account for the observed event luminosities. Based on likelihoods and previously reported TDE candidates, disrupted stars are more likely to be of less than a solar mass ($\sim 0.3 M_{\odot}$), and occur around lower mass BHs ($\sim 10^6$ – $10^7 M_{\odot}$) due to the steeper potential gradient (Gezari et al. 2012; Guillochon & Ramirez-Ruiz 2013). This interpretation then seems quite unlikely in the whole sample of HVAs.

Extinction scenarios have been previously proposed to explain high-amplitude variability in AGN, such as the transition from a Type 1 to Type 1.9 AGN for the object described in LaMassa et al. (2015). L16 noted that whilst the time-scale of such events makes them plausible candidates, there would be a strong colour change expected as the event evolves, which is not observed. A changing optical depth might produce such an effect, such as an eclipse by an opaque cloud. However, as many of the HVAs are observed to be decaying again, this model would consistently require successive extinction events.

The third possible origin of the variability considered in L16 is an accretion rate change. This is difficult to explore, as we do not yet have a model that adequately describes even conventional AGN variability (e.g. Czerny 2004; Lawrence 2012), but in this case, these HVAs could pose an intriguing means of probing extreme accretion rate changes.

The fourth possible origin considered by L16 is a foreground microlensing event. Such a scenario may arise from a star in a foreground galaxy passing between us and a background AGN, increasing the observed flux from the AGN by a large factor. L16 examined this hypothesis, finding that the time-scales and rates expected are approximately consistent with those observed in HVAs. Some of the long-term light curves look like the symmetric, cuspy shapes naively expected from point source–point lens models (e.g. Schmidt & Wambsganss 2010), or the double-peaked structure expected from binary lenses or lenses sheared by the parent galaxy of the lensing star (e.g. Chang & Refsdal 1984). Others show erratic light curves that probably are not caused by microlensing. Bruce et al. (2017), after a detailed treatment of a simple microlensing scenario, show that this is a plausible explanation for at least a subset of these objects.

Overall, one could make a distinction between models where the large outbursts are intrinsic, such as accretion rate changes, and those where the cause is extrinsic, such as extinction or microlensing.

1.3 Aims of this paper

In this paper, we report the optical spectra and light curves, X-ray spectra, and SEDs of four HVAs for which we have obtained *XMM-Newton* observations. We obtain BH mass estimates for each source from the Mg II emission line, and fit SED models to constrain the mass accretion rates. Our primary aim is simply to examine the broad-band properties of the objects in order to establish whether the HVAs appear unusual when compared to other AGN. We do not aim to explicitly test either the accretion instability or microlensing

models, or other specific models. Rather, we examine the observations in the context of the likely differences between possible intrinsic and extrinsic explanations in general.

2 SAMPLE AND OBSERVATIONS

Pan-STARRS 1 (PS1) is a 1.8 m wide-field telescope, situated on the Hawaiian island of Maui, that was originally designed for the detection of near-Earth objects (Kaiser 2004). It saw first light in 2007, and the science mission commenced in 2010. Since 2010 March, it has surveyed the sky in five photometric bands (g_{P1} , r_{P1} , i_{P1} , z_{P1} , and y_{P1}); 56 per cent of the observing time is devoted to the 3π survey, with additional, deeper observations of smaller sky regions making up the ‘Medium Deep Survey’ (Kaiser et al. 2010; Magnier et al. 2013).

The means of selecting our full sample of transients is described in detail in L16. In summary, the parent sample was selected by comparing PS1 magnitudes in the Faint Galaxy Supernova Search (FGSS) data base (Inserra et al. 2013) to earlier SDSS DR7 observations (York et al. 2000; Abazajian et al. 2009). SDSS detections were required to be coincident in position to within 0.5 arcsec, classified as galaxies, and show a ≥ 1.5 mag increase in brightness when re-observed by PS1.

The SDSS and PS1 FGSS photometry were supplemented with existing data from the Catalina Real-time Transient Survey (CRTS; Drake et al. 2009) when available. Pointed follow-up observations with the Liverpool Telescope (LT) at the Roque de los Muchachos Observatory on La Palma were also made, starting in 2011. This additional photometry was used to reject probable SNe by applying both colour cut and decay time criteria (see also Lawrence et al. 2012). This results in an ever-growing sample of HVAs, with 76 discovered so far.

Optical spectra were obtained using the William Herschel Telescope Intermediate dispersion Spectrograph and Imaging System (WHT/ISIS) for much of the sample over several epochs. The data collection and reduction is described in L16 and Bruce et al. (2017). Spectra were normalized to the LT g -band light curve, to mitigate uncertainty in the flux calibration.

We observed four representative, but bright, HVAs with *XMM-Newton* during 2013 August to 2014 February, and this forms the sample examined in this paper. The objects’ names, positions, redshifts, and *XMM* observation details are listed in Table 1. Where possible, observations were split between two epochs to look for variability.

The *XMM-Newton* Pipeline Processing System (PPS) products were extracted from the *XMM-Newton* Science Archive. The PPS uses tasks from the science analysis system to extract events, using only ‘good’ observation time where the background effects and flares were minimal. Our objects are not extended, and are not bright enough for pile-up to occur. A fuller discussion of the PPS data reduction procedure is given in Watson et al. (2009).

Throughout this paper, we will use all available data for each object from the European Photon Imaging Camera (EPIC) MOS1, MOS2, and PN detectors. This will maximize the signal-to-noise (SNR) of the X-ray spectrum.

3 LIGHT CURVES

Long-term light curves are shown in Fig. 1. Two of the objects (J0312 and J1422) show slow smooth outbursts by 1–3 mag, with superimposed variability. J1519, and possibly J1422, shows evidence for two (or more) peaks. This is expected in a binary, or

Table 1. The names (used in this paper), positions, redshifts, *XMM* observation IDs, and observation dates for the sample of four HVAs.

Name	RA (J2000)	Dec. (J2000)	z_{meas}^a	<i>XMM</i> Obs ID(s)	Obs UT(s)
J0312+1836	03 12 40.86	+18 36 41.1	0.889	(0724440) 101 and 601	2013-08-12 and 2014-01-22
J1422+0140	14 22 32.45	+01 40 26.7	1.078	(0724440) 301 ^b and 801	2014-01-04 and 2014-02-06
J1519+0011	15 19 43.99	+00 11 47.4	0.530	(0724440) 401 and 901	2014-01-27 and 2014-02-10
J2232−0806	22 32 10.51	−08 06 21.2	0.276	(0724441) 001 and 101 ^b	2013-12-14

Notes. ^aRedshift measurement described in Section 4.

^bObs IDs 0724440301 and 0724441101 did not yield useful data, possibly due to background activity.

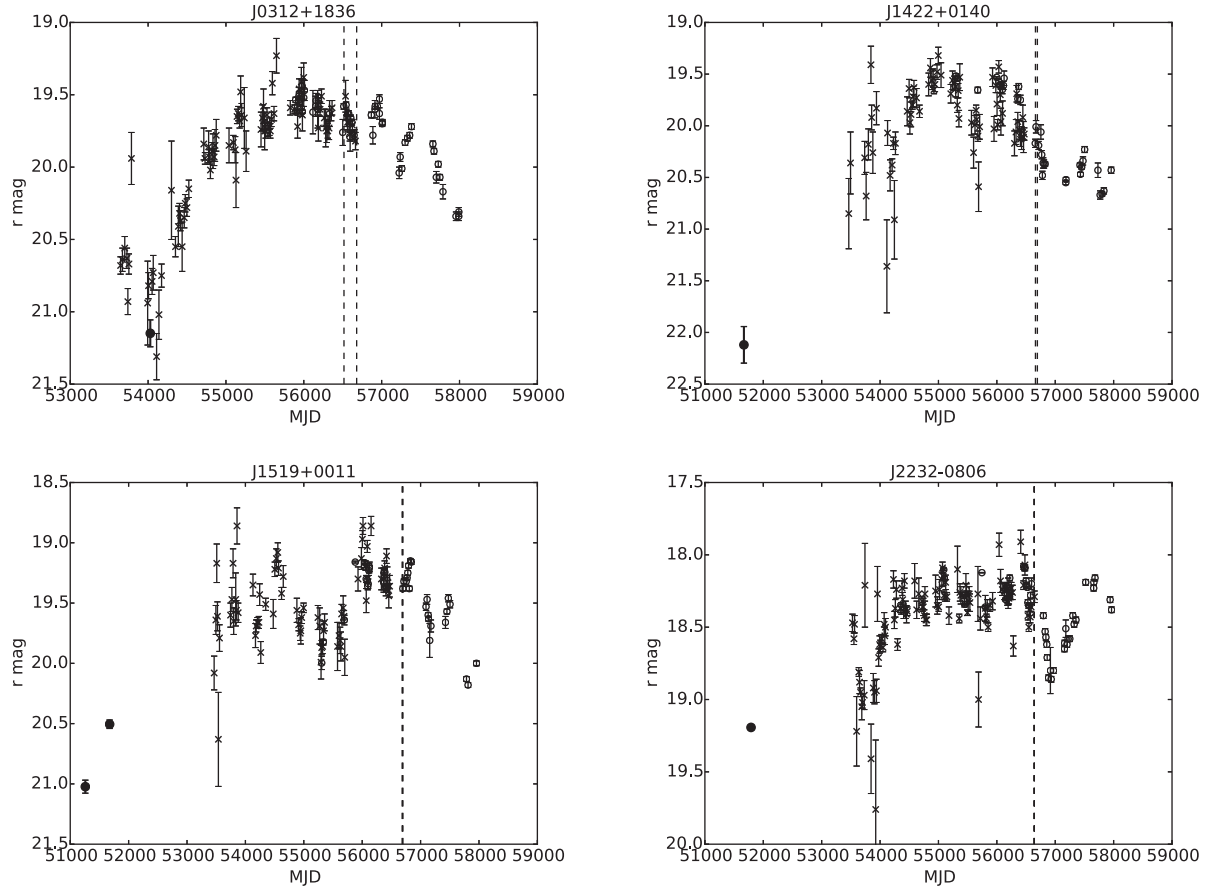


Figure 1. The long-term light curves for the four HVAs. The open circles are Pan-STARRS and LT data; the filled circles are SDSS data; the crosses are CRTS data. The dates of the *XMM* observations are also marked (vertical dashed lines), and there is likely to be only a small, if any, change in flux between observations, for those objects that were observed on two different epochs.

sheared ‘Chang–Refsdal’, microlensing scenario, though it is not our intention to test this hypothesis at this stage. The key point is that for all of J0312, J1422, and J1519, it looks like the low state may be the normal one. The fourth object (J2232) looks rather different, showing a flat top with dips. In this case, it may be that the high state is the normal one.

For this study, we use spectral data from a range of dates to estimate the BH mass (M_{BH}), and then fit the broad-band SED with an energy-conserving accretion model (Done et al. 2012). However, as these HVAs are variable, we first require estimates of the largest and smallest magnitudes, corresponding to the faint and bright states, respectively. For this, we use the *r* band, as it is close to the middle of the spectral range, and corresponds to the same, or a very similar bandpass in PS1, LT, and SDSS. We shift the CRTS magnitudes to match the SDSS/PS1/LT *r* magnitudes,

as observations made by CRTS are in white light, calibrated to a *V*-band zero-point.

We wish to make an estimate of the magnitude of each HVA at the time of the *XMM* observation. As LT photometry exists both prior and subsequent to the *XMM* observations, we linearly interpolate these observations to estimate the magnitudes at these epochs. We estimate the error using a bootstrap technique, whereby 1000 random data sets are drawn from the LT data. These are presented in Fig. 2. We tabulate the *r*-band magnitudes from this analysis in Table 2.

In Fig. 2, we do see evidence for statistically significant variability on top of the global variability trend in some objects. However, for objects with two *XMM* observations, there is no evidence, from the optical light curve, for a change in magnitude between the two *XMM* observation dates (Table 2).

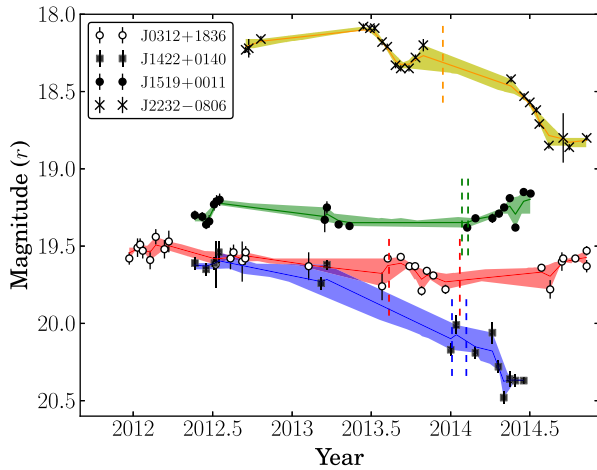


Figure 2. The LT light curves for the four HVAs. We use linear interpolation to measure the magnitude at the epoch of *XMM* observation, and utilize a bootstrap subsampling technique to estimate the 1σ error (shaded regions) on these measurements. The dates of the *XMM* observations are again marked by vertical dashed lines. On this scale, it appears that there is statistically significant intrinsic variability, on top of the global variability, in some objects.

4 BLACK HOLE MASSES

The optical SED of AGN matches well the emission expected from a geometrically thin, optically thick accretion disc (AD) of gas (e.g. Shakura & Sunyaev 1973; Davis, Woo & Blaes 2007). The energy output is thermally dominated; each radius emits blackbody radiation of characteristic temperature that increases to smaller radii, and the peak disc temperature depends on M_{BH} , mass accretion rate, and spin. Modelling the SED therefore requires an estimate of M_{BH} .

This can be accomplished by several methods, the most accurate of which is reverberation mapping (RM; see Blandford & McKee 1982 for original description, and e.g. Peterson et al. 2004; Denney et al. 2010 and Du et al. 2014 for applications). However, RM requires long-term spectroscopic monitoring and thus we are unable to apply it to our sample. Instead, we base our M_{BH} estimates on single-epoch observations of the broad emission lines, using methods calibrated from RM. This approach requires the linewidth to obtain a Keplerian velocity, and a simultaneous luminosity, which determines the radius at which the line is emitted [the so-called broad-line region (BLR) size]. The orbital velocity at that radius then implies a central mass (e.g. Wandel, Peterson & Malkan 1999; Kaspi et al. 2000; Vestergaard 2002; Bentz et al. 2006).

As we only have WHT/ISIS spectra covering optical wavelengths, we must use the Mg II line in the three highest redshift objects, and apply the method of McLure & Dunlop (2004). For the lower redshift J2232–0806, we can make an estimate of M_{BH} using

the well-studied Balmer emission lines, $\text{H}\alpha$ and $\text{H}\beta$, and the methods of Greene & Ho (2005) and Woo & Urry (2002), respectively.

We correct these spectra for Milky Way (MW) reddening, using the dust maps of Schlegel, Finkbeiner & Davis (1998) and the extinction law of Cardelli, Clayton & Mathis (1989), and then decompose the broad emission lines using the following standard procedures, as described in e.g. Greene & Ho (2004), Wang et al. (2009), Shen & Liu (2012), and Matsuoka et al. (2013). The underlying optical continuum in AGN closely approximates to a power law over limited wavelength ranges, and the profiles of the broad emission lines can be modelled by a combination of Gaussian components. The blended Fe II emission observed in many AGN can also be modelled using templates derived from local AGN.

As these HVAs have by definition undergone a significant increase in brightness not typical of AGN, determining the luminosity for the M_{BH} calculation is model dependent. On the one hand, we could assume that the observed (high) flux is the intrinsic level, and the corresponding continuum/line luminosity gives the best representation of the BLR size. For this case, we therefore use the WHT spectra as observed, applying no scaling factor. Alternatively, if the variability is caused by some extrinsic factor, then the normal continuum level would be below that observed. For this situation, we should calculate the continuum/line luminosity from the spectra normalized to the HVA quiescent state, taken to be represented by the SDSS magnitude. Table 2 illustrates the agreement between these two methods.

We then fit the following components.

(i) The continuum underneath the emission lines is modelled as a power law of the form $F(\lambda) = C_1(\lambda/5100 \text{ \AA})^{-C_2}$, where C_1 and C_2 are free constants representing the normalization and slope, respectively. We do not model the Balmer continuum, which could contribute to the continuum under Mg II , as we only use a small part of the spectrum around the Mg II line itself, and the power-law approximation is sufficient.

(ii) The blended Fe II emission is modelled using the template of Véron-Cetty, Joly & Véron (2004) in the optical, and Vestergaard & Wilkes (2001) in the UV, both of which are derived from studies of the Type 1 AGN I Zwicky 1. This component has two free parameters: the normalization and width of the convolving Gaussian.

(iii) Emission lines are modelled as a sum of Gaussians. In the first three objects, of higher redshift, we model only Mg II , with two Gaussian components. We do not attach a physical significance to these components and do not try to model the Mg II line as a doublet, for the same reason as Shen & Liu (2012); the line splitting is too small to be significant. For J2232–0806, we model $\text{H}\alpha$ and $\text{H}\beta$ with three components each (one narrow and two broad), which are locked together in velocity width and amplitude ratio. We also model the narrow $[\text{O III}]$ doublet with two components for each member, and the two lines are fixed at a 2.98:1 ratio (Storey &

Table 2. The key r -band magnitudes for the four HVAs, including the faint state, and at the times of *XMM* observation. The means by which we measure each, as discussed in the text, is shown in parentheses. We also show Δm , the magnitude difference between *XMM* observation and quiescent state. This is the difference in brightness between the two scenarios we test in this paper.

Name	$m_{\text{min, SDSS}}$ (SDSS)	$m_{(XMM1)}$ (Interpolation)	$m_{(XMM2)}$ (Interpolation)	$\Delta m =$ $m_{\text{min, SDSS}} - m_{(XMM1)}$
J0312+1836	21.26 ± 0.06	$19.62^{+0.07}_{-0.04}$	$19.72^{+0.04}_{-0.05}$	1.64
J1422+0140	22.12 ± 0.18	$20.10^{+0.07}_{-0.10}$	$20.12^{+0.06}_{-0.10}$	2.02
J1519+0011	21.02 ± 0.05	$19.35^{+0.03}_{-0.04}$	19.35 ± 0.03	1.67
J2232–0806	19.193 ± 0.016	18.31 ± 0.06	–	0.88

Zeppen 2000). Finally, we model He II with one component. We do not model the narrow [N II] doublet that is often seen on top of the H α profile, as there is no detected [S II] doublet redwards of H α , which indicates that [N II] contribution will be similarly negligible. The narrow components in H α and H β are fixed to the same velocity width as [O III].

Redshifts were measured from the Mg II (J0312+1836, J1422+0140, and J1519+0011) and strong [O III] lines (J2232–0806). These are given in Table 1. M_{BH} is then calculated according to the following equations. We use the relation in McLure & Dunlop (2004) for Mg II (in the first three, higher redshift, objects):

$$M_{\text{BH}} = 3.2 \times \left(\frac{\lambda L_{\lambda}}{10^{44} \text{ erg s}^{-1}} \right)^{0.62} \left(\frac{\text{FWHM}_{\text{MgII}}}{\text{km s}^{-1}} \right)^2 M_{\odot} \quad (1)$$

with λL_{λ} being the monochromatic continuum luminosity at 3000 Å.

In J2232–0806, for H α , we use the method described in Greene & Ho (2005):

$$M_{\text{BH}} = (2.0^{+0.4}_{-0.3}) \times 10^6 \times \left(\frac{L_{\text{H}\alpha}}{10^{42} \text{ erg s}^{-1}} \right)^{0.55 \pm 0.02} \left(\frac{\text{FWHM}_{\text{H}\alpha}}{10^3 \text{ km s}^{-1}} \right)^{2.06 \pm 0.06} M_{\odot}. \quad (2)$$

For comparison purposes, in J2232–0806, we also use the Woo & Urry (2002) method of measuring mass from H β , as an additional check of systematic uncertainties in the value:

$$M_{\text{BH}} = 4.817 \times \left(\frac{\lambda L_{\lambda}}{10^{44} \text{ erg s}^{-1}} \right)^{0.7} \left(\frac{\text{FWHM}_{\text{H}\beta}}{\text{km s}^{-1}} \right)^2 M_{\odot}, \quad (3)$$

where λL_{λ} is the monochromatic continuum luminosity at 5100 Å.

Multiple spectra were available for each object (between three and five), and we performed our spectral analysis on each, measuring M_{BH} from each spectrum independently and taking the mean as our best estimate. The standard deviation of these provides an estimate of the measurement uncertainty, which, it should be noted, is not the dominant source of error on such estimates. Example spectral decompositions are shown in Fig. 3, and the resulting M_{BH} estimates are tabulated, together with observation dates, in Table 3. We use a Levenberg–Marquardt minimization algorithm to fit the data, and employ a sigma-clipping routine in J1422+0140 to reduce the effect of the narrow absorption features we observe in that spectrum. As discussed above, we tabulate M_{BH} values for two cases: one in which the spectra were taken as observed, and the other in which the spectra were scaled to the faint state.

In principle, the two different approaches for estimating M_{BH} could provide additional diagnostics. M_{BH} is constant between observations; therefore, if the continuum varies between WHT observations, the BLR ought to respond to this change. So in the event of the central engine becoming more luminous, the BLR would originate further from the source, and correspondingly the line velocity width would be smaller. Since for the intrinsic case we analyse the spectra as observed, and for the extrinsic case we scale to the quiescent state (which alters the continuum luminosity, but not the linewidth), it is possible that the M_{BH} estimates would be more closely grouped between epochs for the favoured model. However, we see no evidence for such an effect – the scatter arising from the method is too great.

The absorption features in J1422+0140 are consistent with an intervening system. Whilst the doublet on the blue wing of the Mg II profile (at 2750 Å) is likely Mg II absorption in an outflowing

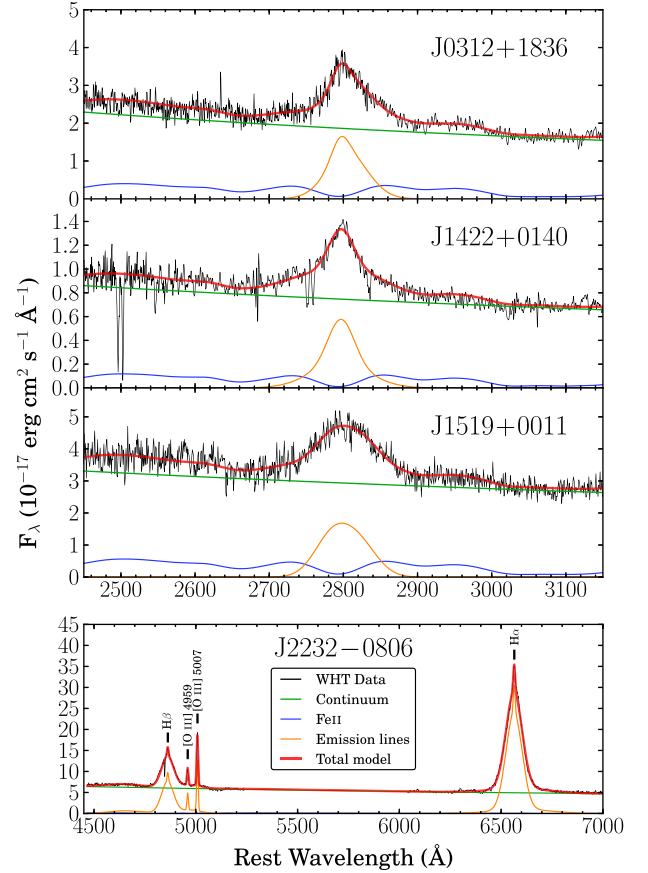


Figure 3. Examples of our model fits to the optical spectrum of each object. In black are the data from WHT/ISIS, and red is the fitted model profile, with constituent components shown. The top three panels show the higher redshift objects, for which only Mg II is available for fitting, and the bottom panel shows J2232–0806, in which we can model H α and H β , in addition to the narrow [O III] doublet; these are marked. We fitted these models to every spectrum for each object (across multiple dates) and took the average as our best estimate. In the bottom panel, we masked out a region of the spectrum between H α and H β , as it contained telluric sky features that would have affected the fitting. The cases shown here are for the spectra normalized to the quiescent state.

component intrinsic to the AGN, the second doublet seen at 2500 Å in Fig. 3 is either Mg II absorption in an extreme outflow (at 0.1c) or more probably in an intervening system at $z \simeq 0.855$. This could be a signature of the lens host galaxy, in the microlensing scenario. More discussion and interpretation of these features are presented in Bruce et al. (2017).

5 X-RAY SPECTRUM AND VARIABILITY

We first carry out an analysis of the X-ray spectrum only, by fitting an absorbed power law to the X-ray spectral data. This model is simple, but at the redshift of these objects we anticipate that it will be appropriate, given the relatively low count numbers. We incorporate absorption components attributable to both the MW (fixed) and the host galaxy (free). We are able to test for any statistically significant variability between observations in J0312+1836 and J1519+0011 – the two objects for which we have usable data from two epochs. MW N_{H} values come from the Leiden/Argentine/Bonn survey (Kalberla et al. 2005). We use the XSPEC spectral analysis package, and a Levenberg–Marquardt minimization routine for all fitting.

Table 3. The key line properties for the sample, including full width at half-maximum (FWHM), continuum/line luminosity, and inferred M_{BH} (according to equations 1–3). The error on the M_{BH} is a measurement error only, and does not reflect systematic errors and uncertainties inherent in the method. We present M_{BH} values resulting from analysing the spectrum as observed (used in scenario A; see Section 6.2) and from normalizing the spectra to the quiescent state (SDSS) magnitude (used for scenario B).

Name	Line	FWHM (km s ⁻¹)	λL_{λ} or L_{line} [log (erg s ⁻¹)] (observed; A)	λL_{λ} or L_{line} [log (erg s ⁻¹)] (quiescent; B)	$M_{\text{BH, observed}}$ [log (M _⊙)] (A)	$M_{\text{BH, faint}}$ [log (M _⊙)] (B)
J0312+1836	Mg II	6000 ± 400	45.09 ± 0.07	44.330 ± 0.011	8.73 ± 0.03	8.26 ± 0.06
J1422+0140	Mg II	4800 ± 400	45.01 ± 0.17	44.146 ± 0.005	8.47 ± 0.10	7.95 ± 0.08
J1519+0011	Mg II	8100 ± 200	44.79 ± 0.07	44.004 ± 0.013	8.81 ± 0.07	8.33 ± 0.03
J2232–0806	H α	4350 ± 70	43.08 ± 0.12	42.76 ± 0.08	8.20 ± 0.05	8.03 ± 0.04
	H β	4350 ± 70	44.20 ± 0.15	43.852 ± 0.011	8.08 ± 0.10	7.86 ± 0.02

Table 4. The X-ray spectra model properties. Photoelectric absorption components for both the MW (fixed) and the host galaxy (free) are modelled. In some observations, the host galaxy absorption is poorly constrained, due to both the redshift and number of counts. The EPIC count errors are 1σ , and the errors on the model parameters are the 90 per cent confidence limits, in line with convention in X-ray astronomy. We also quote Γ and its uncertainty to two decimal places. The exposure time is the full observation time on target, including time that was determined by the *XMM* pipeline to be ‘bad’.

Name	Obs. UT	Exp. time (s)	<i>XMM</i> EPIC Cts	$N_{\text{H, MW}}$ ($\times 10^{20}$ cm ⁻²)	$N_{\text{H, int}}$ ($\times 10^{20}$ cm ⁻²)	Γ	Norm (1 keV) ($\times 10^{-6}$ Ph. / cm ² s keV)	χ^2_{red}
J0312+1836	2013-08-12	35 100	1130 ± 40	8.02	0 ⁺⁶ ₋₀	2.26 ^{+0.14} _{-0.12}	24.6 ^{+1.9} _{-1.5}	0.99
	2014-01-22	29 500	205 ± 16	8.02	10 ⁺⁴⁰ ₋₁₀	2.46 ^{+0.57} _{-0.36}	16 ⁺⁷ ₋₄	1.70
J1422+0140	2014-02-06	34 500	1320 ± 40	2.57	0 ⁺¹⁴ ₋₀	1.73 ^{+0.18} _{-0.09}	15.6 ^{+2.2} _{-0.9}	1.12
J1519+0011	2014-01-27	23 700	4250 ± 70	4.57	0 ⁺² ₋₀	1.96 ^{+0.06} _{-0.05}	90 ⁺⁴ ₋₃	1.01
	2014-02-10	28 000	4850 ± 70	4.57	0.0 ^{+0.9} _{-0.0}	2.04 ± 0.05	80 ⁺² ₋₂	1.05
J2232–0806	2013-12-14	29 500	9300 ± 100	4.11	0.0 ^{+0.4} _{-0.0}	2.21 ± 0.04	284 ± 7	1.10

The X-ray exposure times and count values are shown in Table 4, together with the fitted parameters and 90 per cent confidence limits.

The intrinsic N_{H} in each object is low. This may be because our HVAs are at moderate redshifts, so only the tail of the photoelectric absorption profile is sampled by the X-ray spectrum, and have relatively low count numbers, increasing the uncertainty on $N_{\text{H, int}}$. A specific example of this is evident in the second observation of J0312+1836, where the observation with just ~ 200 counts shows a broad 90 per cent confidence limit on $N_{\text{H, int}}$.

We observe a range in power-law slopes (Γ). Flat power-law slopes are characterized by $\Gamma = 2$, as seen in J1519+0011, soft slopes by $\Gamma > 2$, as seen in J0312+1836 ($\sim 3\sigma$ significance) and J2232–0806 ($\sim 9\sigma$ significance), and hard slopes by $\Gamma < 2$, which we observe in J1422+0140 to a smaller ($\sim 2\sigma$) significance.

There is evidence for statistically significant ($\simeq 4.5\sigma$) variability between the observations of J1519+0011, despite these observations being just 14 d apart. We see that whilst Γ is consistent between the two observations, the normalization has decreased, indicating that the object faded between observations. The optical light curve over the same period (Fig. 2) does not show a significant change, possibly due to larger scatter and insufficient observation cadence. We could therefore be seeing a differentially fading X-ray component in J1519+0011, or this could be due to fast X-ray variability commonly seen in AGN (e.g. Gierliński et al. 2008; Parker et al. 2015). It is possible that the significance of this event could be exaggerated by residual background activity not fully taken into account in the reduction process.

We also test for short-term variability during the observations of each target. Given the relatively low count numbers, this is done by fitting the short-term light curve (~ 100 count bins) with a constant. We only use the ‘good’ on-target time, where background activity was low, and use the full 0.2–12 keV range. Deviation from unity

in the χ^2_{red} fitting statistic can provide evidence for such variability, but we do not observe this in any object. There is therefore no suggestion of statistically significant, short-term X-ray variability in any of the objects.

6 BROAD-BAND SED

6.1 SED construction

In the optical regime, we use the WHT spectrum that was observed closest to the *XMM* observation date, and normalized in the r band to the *XMM* observation epoch (see Section 3). From this spectrum, we define bins expected to be free from emission features (Fe II, emission lines, and the Balmer continuum) as being representative of the continuum flux level. This is discussed in greater detail in Collinson et al. (2015, 2017).

The *XMM* optical monitor (OM) makes UV photometric measurements in a range of optical and UV bands (see Mason et al. 2001). The OM data are expected to be biased high by the presence of emission features in the bandpass of each filter. We correct for this by estimating the flux surplus using the Vanden Berk et al. (2001) quasar template and derived power-law continuum, combined with the effective bandpass of each OM filter at each redshift. By integrating the template over the OM bandpasses to simulate the total flux measured (including emission features) and then integrating the power-law continuum over the same bandpasses to simulate the true continuum level, we estimate the factor by which emission features increase the observed flux in each band. We then scale the OM photometry to correct for this difference, so the OM data represent the continuum flux level. Elvis et al. (2012) demonstrated that variation in the equivalent width of the Lyman α emission feature made utilizing a single value from a template unreliable. Hence, we

did not include the UVM2 band in J0312+1836 in our modelling, as it lies directly on top of Ly α . The correction factor, $f_{\text{corr,OM}}$, was typically $0.8 \lesssim f_{\text{corr,OM}} \lesssim 0.9$, dependent on the filter and redshift of each object.

We do not use data from the Two-Micron All-Sky Survey, UKIRT Infrared Deep Sky Survey, or the *Wide-field Infrared Survey Explorer* to extend the SED into the IR, or the *Galaxy Evolution Explorer* to extend into the UV, as we require quasi-simultaneous data. Also, our objects were often below the detection threshold of these surveys, at the time of observation.

6.2 SED modelling

In this section, we model the broad-band SED of each object. We apply the AGN SED model of Done et al. (2012) – OPTX-AGNF – to each object, fitting to data from *XMM-Newton* (including the onboard OM) and continuum regions of the WHT spectrum. This model comprises three components: accretion disc (AD), soft X-ray excess (SX), and power-law tail (PLT), see Done et al. (2012) for a more detailed explanation. Importantly, the model conserves energy between these components, deriving energy from the release of gravitational potential energy by the accreting gas. We also use multiplicative components to model the extinction and soft X-ray absorption of the MW.

The attenuation variables are the MW extinction, $E(B - V)_{\text{MW}}$ (fixed using values from Schlafly & Finkbeiner 2011), the intrinsic reddening, $E(B - V)_{\text{int}}$ (free), and, as in Section 5, the hydrogen column densities for the photoelectric absorption – $N_{\text{H,MW}}$ and $N_{\text{H,int}}$. Following the procedure described in Collinson et al. (2015), we test SED models both with and without attenuation attributable to the AGN host galaxy. However, as found in that work (see also Capellupo et al. 2015; Castello-Mor, Netzer & Kaspi 2016), the model with host galaxy reddening/absorption produces a better model fit in all cases, when allowing for the additional free parameters. We will therefore consider SED models that include these components from this point onwards. We tested two extinction curve models for the intrinsic reddening: MW and Small Magellanic Cloud. All objects were better fitted with the MW extinction curve, but the difference in χ^2_{red} was marginal between the two cases in J2232–0806.

Due to the redshift of our objects, and the quality of our X-ray data, we do not well sample the SX component with the *XMM* data. In Collinson et al. (2015), it was found that the inclusion of the SX was justified as it was partially sampled in high-mass ($M_{\text{BH}} > 10^9$) objects. However, that sample was of higher redshift ($z > 1.5$), and consequently higher M_{BH} (McLure & Dunlop 2004). For the current sample, we initially applied two versions of the model: one with a dominant SX (initially contributing 70 per cent of the reprocessed energy – e.g. Done et al. 2013; Collinson et al. 2015 – which was then allowed to vary), and one with no SX. We found that in some cases the model including the SX was not physical (e.g. because all AD energy was reprocessed by the SX and PLT). J2232–0806 did show evidence for an improved fit with the SX component (χ^2_{red} of 1.07 compared to 1.11 without the SX component); however, the difference in end result was small. Therefore, in the interest of simplicity and consistency, we opted to use the simplified, two-component (AD and PLT) version of OPTXAGNF.

Using an energetically self-consistent accretion model allows us to compare the two hypotheses (high-state normal or low-state normal, see Section 1.2) for the increase in brightness of these HVAs. If the change is intrinsic, then the spectral data will represent the energy flux of a conventional AGN that has seen an increase in

accretion rate. In the event that the increment in brightness is due to an extrinsic effect, then the intrinsic flux of the AGN must be a significant factor smaller than that we observe, corresponding to a smaller mass accretion rate.

We test these two scenarios, by producing corresponding models for each object.

(A) As observed. The model will be fitted to the data with no additional factors applied.

(B) Change is extrinsic. We descale the SED at all wavelengths to match the SDSS low state.

This enables us to contrast the intrinsic and extrinsic scenarios and look for evidence of unusual effects, by comparing the inferred properties with those of larger AGN samples. As discussed in Section 4, we have estimated M_{BH} for each of these situations, and we will therefore use a different M_{BH} estimate for the two scenarios, which is fixed in the fitting. The resulting model properties are tabulated in Table 5 and the SEDs for both cases are shown in Fig. 4. The only fitted property we do not tabulate is $N_{\text{H,int}}$, as these are all at or close to zero, as in Table 4.

7 DISCUSSION

7.1 SED model

Figs 5–7 show the results from our model fitting, in the context of a large sample of normal AGN (Lusso et al. 2010, hereafter L10).

L10 presented SEDs for a large, X-ray selected sample of 545 Type 1 AGN, drawn from the *XMM-Newton* Cosmic Evolution Survey sample. They estimated the multi-waveband SEDs for their sample using multiple polynomial interpolations and extrapolated power laws through their data in $\log(\nu L_\nu)$ space. This method does not apply any physical considerations to the procedure, but adheres to known constraints (e.g. range of the PLT). We compare our calculated values for $L_{2500\text{\AA}}$, $L_{2\text{keV}}$, and α_{OX} with those in the L10 sample. α_{OX} is an often-used measure of the relative X-ray loudness of an AGN, and is defined as

$$\alpha_{\text{OX}} = -\frac{\log(L_{2\text{keV}}/L_{2500\text{\AA}})}{2.605}. \quad (4)$$

We plot the linear best-fitting relations derived in L10 using the method of Isobe et al. (1990). The ellipses show the 1σ and 2σ error regions for the HVA sample centroid of each tested model. These regions are calculated using a Monte Carlo method, similar to that described in Section 3. The central 68 and 95 per cent of these centroid distributions are an indication of the 1σ and 2σ error boundaries, respectively. To guide the eye, we also overlay contours from a bivariate Gaussian kernel-density estimate of the L10 sample distribution.

In Fig. 5, we also show the linear relations derived in Lusso & Risaliti (2016, hereafter LR16). The LR16 sample comprises 2153 AGN detected in both SDSS and the *XMM* serendipitous source catalogue. They calculate $L_{2\text{keV}}$ from the *XMM* EPIC total energy fluxes, assuming a constant photon index and neutral hydrogen column. $L_{2500\text{\AA}}$ values were provided in the Shen et al. (2011) catalogue. This approach differs from that in L10, but there is agreement between the studies with respect to the $L_{2500\text{\AA}} - L_{2\text{keV}}$ relation. LR16 show that by applying various quality cuts, the dispersion of this relation drops significantly. In Fig. 5, the relation derived from the full LR16 sample is shown by the red dotted line, and the relation emerging from the best-quality subsample (743 objects) by the red long-dashed line.

Table 5. The optimum fitted parameters for the various SED models. Uncertainties quoted are the 90 per cent confidence limits, as is conventional in X-ray astronomy, and are estimated using the Fisher matrix. As such, they are only indicative of the true measurement error. Columns are as follows: (1) object name; (2) the lens factor, if applied – this is a constant factor that multiplies the model flux at all energies and derives from Δm in Table 2; (3) log bolometric luminosity [$\log(\text{erg s}^{-1})$]; (4) log luminosity density at 2500 Å [$\log(\text{erg s}^{-1} \text{ Hz}^{-1})$]; (5) log luminosity density at 2 keV [$\log(\text{erg s}^{-1} \text{ Hz}^{-1})$]; (6) α_{OX} spectral index (e.g. Lusso et al. 2010); (7) intrinsic $(B - V)$ extinction [mag]; (8) reduced mass accretion rate [\dot{M}_{Edd}]; (9) coronal radius [R_g]; (10) outer disc radius [R_g]; (11) PLT spectral index; (12) χ^2_{red} fitting statistic.

Name (1)	f_{lens} (2)	L_{bol} (3)	$L_{2500 \text{ Å}}$ (4)	$L_{2 \text{ keV}}$ (5)	α_{OX} (6)	$E(B - V)$ (7)	\dot{m} (8)	r_{cor} (9)	r_{out} (10)	Γ (11)	χ^2_{red} (12)
<i>Model A: as observed. $M_{\text{BH}} = M_{\text{BH, observed}}$ in Table 3</i>											
J0312+1836	N/A	45.87 ± 0.12	30.25	26.44	1.46	0.07 ± 0.02	0.12 ± 0.03	13 ± 2	93 ± 8	2.24 ± 0.11	1.83
J1422+0140	N/A	45.72 ± 0.10	30.04	26.53	1.35	0.06 ± 0.03	0.12 ± 0.03	20 ± 13	>1000	1.75 ± 0.10	1.15
J1519+0011	N/A	45.8 ± 0.3	30.10	26.50	1.38	0.16 ± 0.06	0.09 ± 0.06	13 ± 4	49 ± 3	2.00 ± 0.03	1.11
J2232–0806	N/A	45.30 ± 0.17	29.49	26.31	1.22	0.00 ± 0.04	0.10 ± 0.04	30 ± 20	120 ± 6	2.20 ± 0.05	1.11
<i>Model B: descaled. $M_{\text{BH}} = M_{\text{BH, faint}}$ in Table 3</i>											
J0312+1836	4.53	45.27 ± 0.14	29.57	25.78	1.46	0.07 ± 0.03	0.08 ± 0.03	12 ± 2	134 ± 13	2.24 ± 0.11	1.83
J1422+0140	6.43	45.0 ± 0.2	29.25	25.72	1.35	0.06 ± 0.05	0.08 ± 0.04	17 ± 6	>1000	1.75 ± 0.09	1.15
J1519+0011	4.66	45.1 ± 0.3	29.40	25.83	1.37	0.15 ± 0.07	0.05 ± 0.04	13 ± 4	71 ± 5	2.00 ± 0.03	1.11
J2232–0806	2.25	44.95 ± 0.09	29.14	25.96	1.22	0.000 ± 0.019	0.065 ± 0.014	29 ± 14	119 ± 7	2.20 ± 0.05	1.11

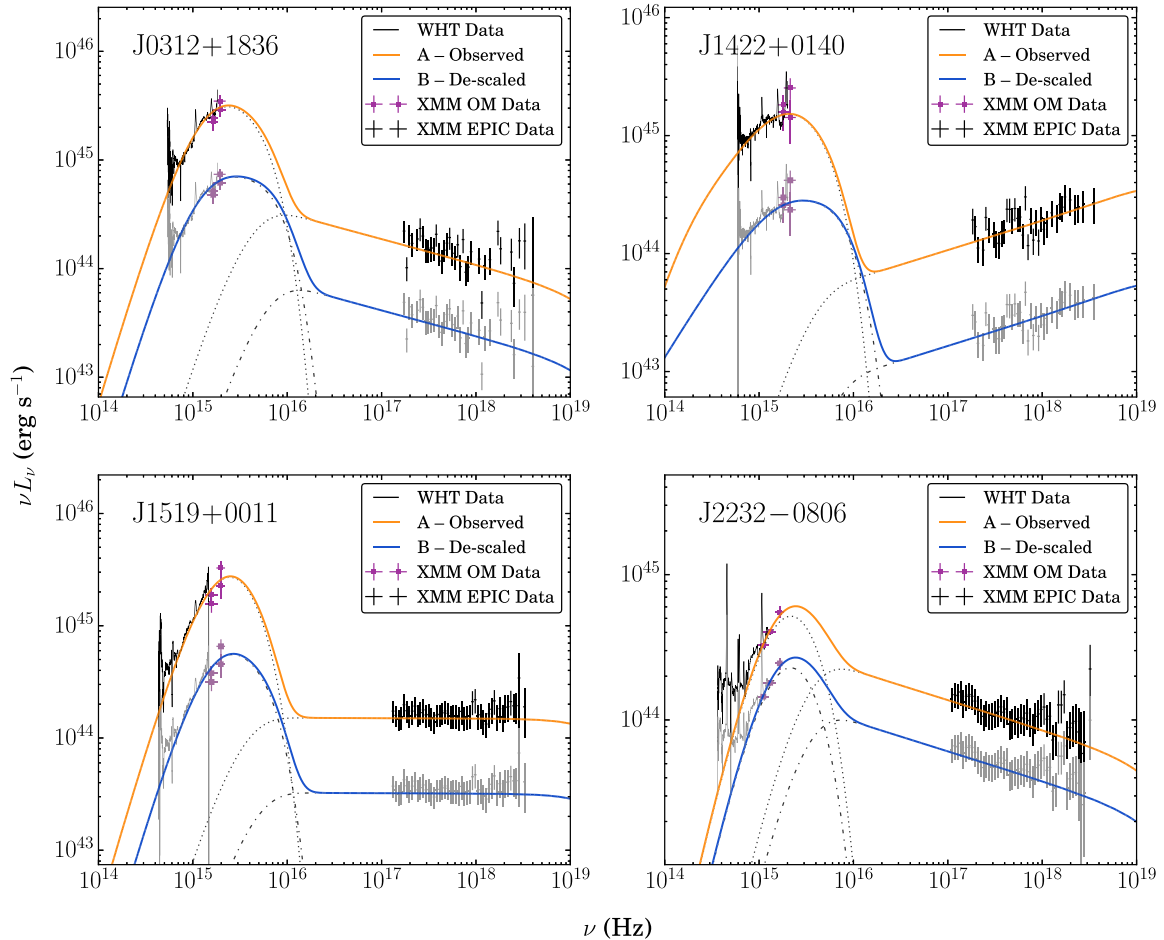


Figure 4. Modelled SEDs for both scenarios. In the extrinsic variability scenario, we assume that the observed data are not representative of the normal state, and that the intrinsic flux is lower than observed. In these plots, we show the intrinsic SED in each case; for model B, we therefore scale the data down to the implied intrinsic flux, shown in grey. Model constituent components (AD and PLT) are shown by the dotted and dash–dotted lines.

The most direct result of this analysis can be seen in Fig. 6. For their observed optical–UV luminosities, the four HVAs are systematically X-ray loud – they all lie under the trend line of Fig. 6. Given the trend of α_{OX} with luminosity, this could be because the luminosities are systematically overestimated. If we apply the

descaling factor estimated from our scenario B model fits, the HVAs fall on the trend line. However, although the result is formally significant at $>2\sigma$, given that we have only four data points, it is hard to be confident of this result. A larger sample of HVAs is clearly desirable.

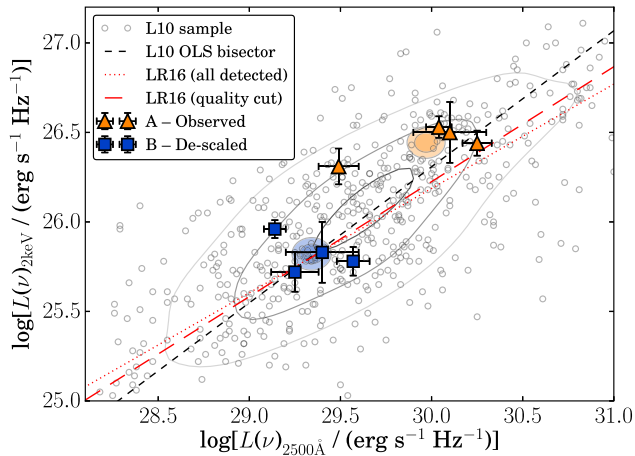


Figure 5. The L10 sample, $L(\nu)_{2\text{keV}}$ against $L(\nu)_{2500\text{\AA}}$ with our sample (blue and orange) overplotted. LR16 relations are also shown. The contours illustrate the distribution of the L10 sample, and the ellipses show the sample centroids (1σ and 2σ significance levels).

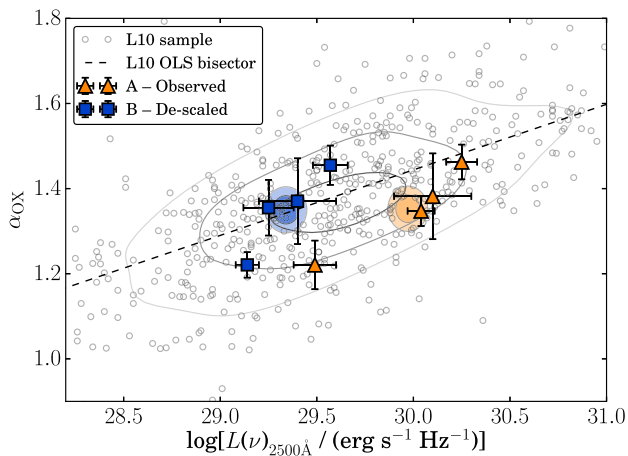


Figure 6. The L10 sample, α_{OX} against $L(\nu)_{2500\text{\AA}}$ with our sample (blue and orange) overplotted.

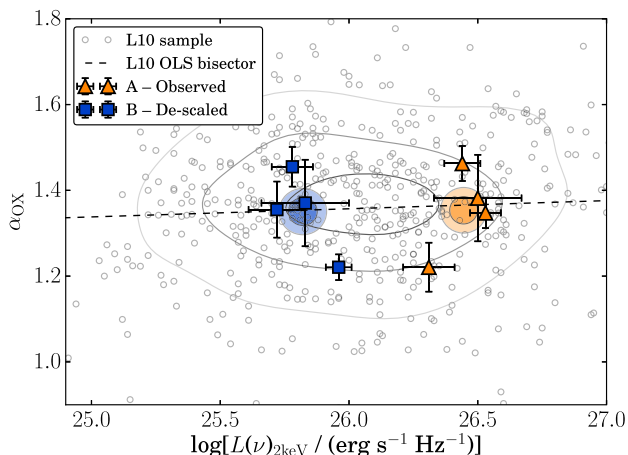


Figure 7. The L10 sample, α_{OX} against $L(\nu)_{2\text{keV}}$ with our sample (blue and orange) overplotted.

The comparison with L10 and LR16 ought to be reasonable; whilst our approaches for calculating the SEDs differ, we are primarily concerned with $L(\nu)_{2500\text{\AA}}$ and $L(\nu)_{2\text{keV}}$ that are well sampled, and thus well defined by our various approaches. Uncertainty may arise in $L(\nu)_{2500\text{\AA}}$ due to differing means of correcting for intrinsic reddening. Owing to the limited quality of their data, L10 make only simple corrections for host galaxy reddening. Unfortunately, AGN samples that utilize more advanced SED models that address these limitations either cover limited redshift ranges (e.g. Jin et al. 2012) or lack X-ray data (e.g. Capellupo et al. 2015), in addition to being much smaller. However, LR16 explore the effects of a number of quality criteria (including reddening) in their large sample of AGN. They find that whilst the dispersion of the $L(\nu)_{2500\text{\AA}}-L(\nu)_{2\text{keV}}$ relation is dependent on such criteria, the relation itself is not. Therefore, our findings should not be affected by this source of uncertainty.

We may also consider the average AGN templates of Jin et al. (2012) as being representative of the archetypal AGN SEDs at different accretion rates, as they use the same model as in this paper, applied to a larger, more local AGN sample. In terms of α_{OX} , as a sample our HVAs appear to most closely resemble the average SED for objects with moderate linewidth. However, even within four objects, we see a broad range of X-ray spectral shapes ($1.8 \lesssim \Gamma \lesssim 2.2$) that almost covers the full range of SEDs observed by Jin et al. (2012). For instance, J0312+1836 shows an unusually soft X-ray spectrum, compared to the average SED in Jin et al. (2012), for an object at the accretion rates predicted in either case. To this end, a more conclusive result would require a larger sample of HVAs with X-ray data.

In both situations, we generally predict moderate intrinsic reddening (mean $E(B-V) \simeq 0.07$, $n = 4$ objects). This is a little higher than typical extinction values determined in Collinson et al. (2015, mean $E(B-V) \simeq 0.04$, $n = 11$ objects) and Capellupo et al. (2015, mean $E(B-V) \simeq 0.02$, $n = 30$ objects). Our sample only comprises four objects, so it is impossible to say that this is a true trend among HVAs. But higher-than-usual extinctions may be expected if there are two galaxies (i.e. both AGN host galaxy and lens host galaxy) extinguishing the optical/UV light. These reddening curves would be at different redshifts (i.e. the host and lens host galaxy), but we would need better data coverage and SNR to deconvolve these two contributions, especially as the total $(B-V)$ extinction we measure is <0.1 mag.

The intrinsic extinction parameter is dependent on the slope of the optical spectrum. Other factors that could affect the spectral slope are the outer AD radius and host galaxy contamination (potentially with an additional lens host galaxy, if these are indeed microlensed AGN). We do not model the host galaxy component in this study, as we do not expect the host galaxy to make a significant contribution to the SED bluewards of $H\beta$ (Shen et al. 2011; Collinson et al. 2017). We tested a version of the model where the outer disc radius was fixed at $1000 R_g$, but in three objects the fit was marginal.

The evidence we see for a fading X-ray component (Section 5) in J1519+0011 is interesting, as if it continued to fade at that rate (i.e. significantly faster than the optical), it could suggest differential magnification of the source, and provide a probe of the corona size. To confirm this would require follow-up observations with *XMM-Newton*.

7.2 Additional uncertainties

There is good agreement between the scaled optical (WHT) data and the corrected (*XMM OM*) UV data, suggesting that it is reasonable both to normalize the WHT spectrum using the optical light curve

and to correct the OM data for emission feature contamination using the Vanden Berk et al. (2001) template and power-law continuum.

It should be noted that in order to estimate M_{BH} in the extrinsic variability case (model B), we scaled each source to the brightness level of the quiescent state, which we assumed to be represented by the SDSS magnitude. However, in the cases where the SDSS observations are dominated by the host (or foreground) galaxy, the AGN flux could be fainter. In this case, M_{BH} would be smaller, meaning an AD that peaks further into the UV, with higher mass accretion rates. Our M_{BH} for the extrinsic case should therefore be considered upper limits.

A final caveat is that if the BHs are spinning, the radius of last stable circular orbit is reduced and a corotating AD can extend closer to the event horizon, shifting the AD peak bluewards. Unfortunately, our data are insufficient to make a judgement of the BH spin (see Collinson et al. 2017).

8 SUMMARY AND CONCLUSIONS

We have presented results from X-ray observations of four extremely variable AGN (termed ‘hypervariable’ AGN or HVAs) discovered in the Pan-STARRS data base (Lawrence et al. 2012; L16). To explain this variability, we consider two distinct scenarios – A and B. In scenario A, this change is intrinsic (e.g. caused by a large increase in mass accretion rate), and in scenario B, the flux has been increased by some extrinsic factor, such as for example foreground microlensing. We explore these two scenarios through an analysis of their SEDs.

We have estimated the magnitudes of each AGN in both faint and bright states, and also at the epoch of the *XMM–Newton* observation, using optical photometry light curves. We then use optical spectra from WHT/ISIS to estimate M_{BH} from the profiles of the broad emission lines Mg II and H α . For scenario A, we analyse the spectra as observed, and for scenario B, we scale them to the faint (assumed to represent the intrinsic) state.

We then fit an energy-conserving, broad-band SED model to the multi-wavelength data for each object. This approach allows us not only to characterize the energetics for each scenario, but also constrains the accretion flow properties, including the SED shape, which is dependent on the mass accretion rate.

We compare the properties of the models for each of the four objects, in both scenarios (A and B) with the L10 and L16 samples. Our four HVAs show distinct groupings of scenarios A and B in SED shape versus luminosity parameter space. In scenario A, we see evidence that the AGN are X-ray loud for their apparent UV luminosities, whereas in scenario B, their X-ray loudness seems normal.

This provides an important additional diagnostic of the expected arrangement of these HVAs. With a larger sample of X-ray observed HVAs, we hope to be able to increase the significance of our findings.

ACKNOWLEDGEMENTS

We would like to thank the referee for constructive comments. We appreciate the help of Marianne Vestergaard, who provided the UV Fe II templates from Vestergaard & Wilkes (2001), and JSC is forever grateful to Edward Shaw for everything he contributed. JSC is funded by Science and Technology Facilities Council (STFC) grant ST/K501979/1 and AB by the Edinburgh PCDS scholarship. MJW and CD are supported by STFC grant ST/L00075X/1.

This research is based on observations obtained with *XMM–Newton*, an ESA science mission with instruments and contributions directly funded by ESA Member States and NASA.

The Pan-STARRS 1 Survey has been made possible through contributions of the Institute for Astronomy; the University of Hawaii; the Pan-STARRS Project Office; the Max Planck Society and its participating institutes, the Max Planck Institute for Astronomy, Heidelberg and the Max Planck Institute for Extraterrestrial Physics, Garching; the Johns Hopkins University; Durham University; the University of Edinburgh; Queen’s University Belfast; the Harvard–Smithsonian Center for Astrophysics; the Las Cumbres Observatory Global Telescope Network, Incorporated; the National Central University of Taiwan; and the National Aeronautics and Space Administration under Grant No. NNX08AR22G issued through the Planetary Science Division of the NASA Science Mission Directorate.

The William Herschel Telescope is operated on the island of La Palma by the Isaac Newton Group. The Liverpool Telescope, also on the island of La Palma, is operated by Liverpool John Moores University with financial support from the UK Science and Technology Facilities Council. Both are in the Spanish Observatorio del Roque de los Muchachos of the Instituto de Astrofísica de Canarias.

Funding for SDSS-III has been provided by the Alfred P. Sloan Foundation, the Participating Institutions, the National Science Foundation, and the US Department of Energy Office of Science. The SDSS-III website is <http://www.sdss3.org/>.

Finally, we are grateful to the contributors to the PYTHON programming language, and HEASARC, for software and services.

REFERENCES

- Abazajian K. N. et al., 2009, *ApJS*, 182, 543
- Alexander D. M., Hickox R. C., 2012, *New Astron. Rev.*, 56, 93
- Bentz M. C., Peterson B. M., Pogge R. W., Vestergaard M., Onken C. A., 2006, *ApJ*, 644, 133
- Blandford R. D., McKee C. F., 1982, *ApJ*, 255, 419
- Bruce A. et al., 2017, *MNRAS*, 467, 1259
- Capellupo D. M., Netzer H., Lira P., Trakhtenbrot B., Mejía-Restrepo J., 2015, *MNRAS*, 446, 3427
- Cardelli J. A., Clayton G. C., Mathis J. S., 1989, *ApJ*, 345, 245
- Castello-Mor N., Netzer H., Kaspi S., 2016, *MNRAS*, 458, 1839
- Chang K., Refsdal S., 1984, *A&A*, 132, 168
- Collinson J. S., 2016, PhD thesis, Durham University
- Collinson J. S., Ward M. J., Done C., Landt H., Elvis M., McDowell J. C., 2015, *MNRAS*, 449, 2174
- Collinson J. S., Ward M. J., Landt H., Done C., Elvis M., McDowell J. C., 2017, *MNRAS*, 465, 358
- Cristiani S., Vio R., Andreani P., 1990, *AJ*, 100, 56
- Czerny B., 2004, preprint ([arXiv:astro-ph/0409254](https://arxiv.org/abs/astro-ph/0409254))
- Davis S. W., Woo J.-H., Blaes O. M., 2007, *ApJ*, 668, 682
- Denney K. D. et al., 2010, *ApJ*, 721, 715
- Done C., Davis S. W., Jin C., Blaes O., Ward M., 2012, *MNRAS*, 420, 1848
- Done C., Jin C., Middleton M., Ward M., 2013, *MNRAS*, 434, 1955
- Drake A. J. et al., 2009, *ApJ*, 696, 870
- Du P. et al., 2014, *ApJ*, 782, 45
- Elvis M. et al., 2012, *ApJ*, 759, 6
- Gezari S. et al., 2012, *Nature*, 485, 217
- Gierliński M., Middleton M., Ward M., Done C., 2008, *Nature*, 455, 369
- Greene J. E., Ho L. C., 2004, *ApJ*, 610, 722
- Greene J. E., Ho L. C., 2005, *ApJ*, 630, 122
- Guillochon J., Ramirez-Ruiz E., 2013, *ApJ*, 767, 25
- Inserra C. et al., 2013, *ApJ*, 770, 128
- Isobe T., Feigelson E. D., Akritas M. G., Babu G. J., 1990, *ApJ*, 364, 104
- Jin C., Ward M., Done C., Gelbord J., 2012, *MNRAS*, 420, 1825

- Kaiser N., 2004, in Oschmann J. M., Jr, ed., Proc. SPIE, Vol. 5489, Ground-based Telescopes. SPIE, Bellingham, p. 11
- Kaiser N. et al., 2010, in Stepp L. M., Gilmozzi R., Hall H. J., eds, Proc. SPIE, Vol. 7733, Ground-based and Airborne Telescopes III. SPIE, Bellingham, p. 77330E
- Kalberla P. M. W., Burton W. B., Hartmann D., Arnal E. M., Bajaja E., Morras R., Pöppel W. G. L., 2005, A&A, 440, 775
- Kaspi S., Smith P. S., Netzer H., Maoz D., Jannuzi B. T., Givon U., 2000, ApJ, 533, 631
- LaMassa S. M. et al., 2015, ApJ, 800, 144
- Lawrence A., 2012, MNRAS, 423, 451
- Lawrence A., Gezari S., Elvis M., Ward M., Smartt S., Smith K., Wright D., 2012, EPJ Web Conf., 39, 3002
- Lawrence A. et al., 2016, MNRAS, 463, 296 (L16)
- Lusso E., Risaliti G., 2016, ApJ, 819, 154 (LR16)
- Lusso E. et al., 2010, A&A, 512, A34 (L10)
- McLure R. J., Dunlop J. S., 2004, MNRAS, 352, 1390
- Magnier E. A. et al., 2013, ApJS, 205, 20
- Mason K. O. et al., 2001, A&A, 365, L36
- Matsuoka K. et al., 2013, ApJ, 771, 64
- Morganson E. et al., 2015, ApJ, 806, 244
- Parker M. L. et al., 2015, MNRAS, 447, 72
- Peterson B. M. et al., 2004, ApJ, 613, 682
- Rees M. J., 1988, Nature, 333, 523
- Salpeter E. E., 1964, ApJ, 140, 796
- Schlafly E. F., Finkbeiner D. P., 2011, ApJ, 737, 103
- Schlegel D. J., Finkbeiner D. P., Davis M., 1998, ApJ, 500, 525
- Schmidt R. W., Wambsganss J., 2010, Gen. Relativ. Gravit., 42, 2127
- Shakura N. I., Sunyaev R. A., 1973, A&A, 24, 337
- Shen Y., Liu X., 2012, ApJ, 753, 125
- Shen Y. et al., 2011, ApJS, 194, 45
- Storey P. J., Zeppen C. J., 2000, MNRAS, 312, 813
- Vanden Berk D. E. et al., 2001, AJ, 122, 549
- Véron-Cetty M.-P., Joly M., Véron P., 2004, A&A, 417, 515
- Vestergaard M., 2002, ApJ, 571, 733
- Vestergaard M., Wilkes B. J., 2001, ApJS, 134, 1
- Wandel A., Peterson B. M., Malkan M. A., 1999, ApJ, 526, 579
- Wang J.-G. et al., 2009, ApJ, 707, 1334
- Ward M., Elvis M., Fabbiano G., Carleton N. P., Willner S. P., Lawrence A., 1987, ApJ, 315, 74
- Watson M. G. et al., 2009, A&A, 493, 339
- Woo J.-H., Urry C. M., 2002, ApJ, 579, 530
- York D. G., Adelman J., Anderson J. E., Jr, Anderson S. F., Annis J., SDSS Collaboration, 2000, AJ, 120, 1579

This paper has been typeset from a \LaTeX file prepared by the author.